

Turbulent transport in supersonic film cooling with helium injection

Pascal Marquardt^{1*}, Michael Klaas¹, Wolfgang Schröder¹

¹ RWTH Aachen University, Institute of Aerodynamics, 52062 Aachen, Germany

* p.marquardt@aia.rwth-aachen.de

Abstract

A supersonic film-cooling configuration with cold helium injection is experimentally investigated by high-speed particle-image velocimetry (PIV). A laminar, cooled helium flow is injected at a Mach number $Ma_i = 1.3$ beneath a turbulent boundary layer of an air flow at a freestream Mach number $Ma_\infty = 2.45$. The total temperature ratio between the cooling film and the freestream is $T_{0,i}/T_{0,\infty} = 0.75$. The static pressure of the cooling film matches the freestream condition. Two flow cases are considered, i.e., one undisturbed flow and one flow with shock interaction. In the shock interaction case, a flow deflection of $\beta = 8^\circ$ generates a shock that impinges upon the cooling film flow 52 nozzle heights downstream of the injection position. Without shock interaction, the high injection velocity of the cooling film leads to turbulent transport off the wall in the mixing layer between the cooling film and the outer shear layer which is beneficial for cooling applications. However, an impinging shock generates a large separation bubble that leads to intense turbulent mixing. The turbulent transport towards the wall with shock interaction is up to 18 times higher than in the undisturbed reference case.

1 Introduction

The injection of cold gas along the surface, so-called film cooling, is a common cooling method in supersonic applications with high thermal loads, e.g., scramjet combustors, where the gas temperature exceeds the thermal limit of the surface material. As shown in the review of Goldstein (1971), a promising cooling concept for supersonic flows is a cooling configuration with tangential injection. A schematic drawing of this cooling concept beneath a turbulent boundary layer is shown in figure 1. According to Seban and Back (1962) and Juhany and Hunt (1994), the flow can be divided into three main regions. The first region is the potential core right downstream of the injection, which is bounded by the mixing layer being shed from the lip and the slot flow boundary layer. The potential core ends where the mixing layer and the slot-flow boundary layer merge. The wall-jet region, which is characterized by intense mixing, starts at this location. Further downstream, the flow relaxes to an undisturbed turbulent boundary layer which is denoted as boundary-layer region.

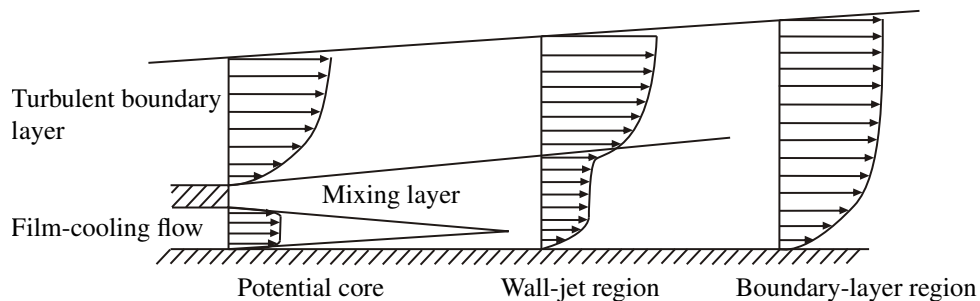


Figure 1: Flow schematic with velocity profiles indicating three distinct flow regions (Seban and Back (1962); Juhany and Hunt (1994)) in a tangential film-cooling configuration (Konopka et al. (2012)).

In the following, a brief overview of the literature on film cooling flows is given. Early studies on shock/cooling-film interaction focused on the analysis of the wall heat flux. Experimental and numerical studies of a helium injection into a turbulent boundary layer at a freestream Mach number $Ma_\infty = 6.4$ were conducted by Kamath et al. (1990). The cooling film was injected with an injection Mach number $Ma_i = 3$. The shocks impinging on the cooling film were generated by flow deflections of 5.5° , 8° , and 10.5° . The Reynolds-averaged Navier-Stokes (RANS) simulations and the measurements of the wall heat flux indicated a small reduction of heat flux by the cooling film. Holden et al. (1990) performed experiments in a shock tunnel at a freestream Mach number $Ma_\infty = 6$ and injection with an injection Mach number $Ma_i = 3$. Shocks generated by either 10° , 15° , or 20° flow deflection impinged upon the cooling film. The authors concluded that film cooling has little or no effect on the peak heat transfer. Olsen et al. (1990) conducted experimental investigations of a helium injection with injection Mach number $Ma_i = 3$ into a turbulent boundary layer at a freestream Mach number $Ma_\infty = 6.4$. The authors found that the shock impingement position has no effect on the peak heat flux. However, they did not state in which flow region their measurements were made. Juhany and Hunt (1994) concluded that the differences in the literature are related to the flow region where the shock impinges upon the cooling film. They performed experimental investigations of a shock/cooling-film interaction in the wall-jet region and in the boundary-layer region with air injection Mach numbers $Ma_i = 1.2$ and 2.2 and helium injection Mach numbers $Ma_i = 1.3$ and 2.2 at a freestream Mach number $Ma_\infty = 2.44$. Juhany and Hunt (1994) found a weak influence of the shock interaction on the temperature of the wall as long as no separation occurs. Konopka et al. (2012, 2013a) performed large-eddy simulations (LES) of shock/cooling-film interaction in the potential core and the boundary-layer region for injection Mach numbers $Ma_i = 1.2$ and 1.8 . They found a shock induced decrease of the cooling effectiveness that depends on the Mach number and the impingement position. While the low Mach number case showed a stronger decrease with shock impingement in the boundary-layer region, the high Mach number case exhibited a higher cooling effectiveness decrease with shock interaction in the potential core. Further numerical investigations of Konopka et al. (2013b) included film cooling with hydrogen and helium injection at an injection Mach number $Ma_i = 1.3$. The LES results showed that even though the separation bubble is larger at hydrogen injection, the cooling effectiveness of the hydrogen film is superior to that of the helium film.

The analysis of the literature shows that the experimental investigations on shock/cooling-film interaction mainly utilize pitot probes, wall heat flux measurements, and schlieren visualizations. Measurement techniques that captured extended regions of the velocity field were used by Marquardt et al. (2019, in press), who performed experimental investigations of shock/cooling-film interaction using high-speed particle-image velocimetry (PIV). They conducted experiments for isoenergetic injection with injection Mach numbers $Ma_i = 1.2$ and 1.8 and flow deflection angles of $\beta = 5^\circ$ and $\beta = 8^\circ$. They found a high sensitivity of the flow structure to the injection Mach number, and, hence, to the near-wall momentum. Increased momentum led to less pronounced separation and significantly decreased turbulent mixing. However, the measurements were performed at isoenergetic air injection. Hence, it is unclear how the results transfer to realistic application scenarios, where the injection to freestream temperature ratio is below unity to provide any cooling effect. PIV and temperature measurements at cold injection were performed by Marquardt et al. (2018). They investigated the injection of cold air at a temperature ratio $T_{0,i}/T_{0,\infty} = 0.8$ and an injection Mach number $Ma_i = 1.2$. A flow deflection of $\beta = 5^\circ$ generates a shock that impinges upon the cooling film. The investigated cases show no or little shock induced separation. Nevertheless, shock impingement led to an increased turbulent transport towards the wall and higher temperatures in the cooling film close to the wall.

In some application scenarios, hydrogen fuel is considered as cooling fluid. To account for the large density difference between the cooling film and the freestream, it is the scope of this study to provide high-resolution velocity measurements of a cooled helium injection into an air freestream. For this, a supersonic, laminar helium jet is injected underneath a turbulent boundary layer of an air freestream at a freestream Mach number of $Ma_\infty = 2.45$. Like in the experiments of Juhany et al. (1994), Juhany (1994), and Konopka et al. (2013b) the cooling film is injected at an injection Mach number $Ma_i = 1.3$ at a total temperature ratio of $T_{0,i}/T_{0,\infty} = 0.75$. A shock is generated by a flow deflection of $\beta = 8^\circ$ and impinges upon the cooling film 52 nozzle heights downstream of the injection. In addition to the shock interaction case, a reference case without shock interaction is considered in this study. First, the undisturbed reference case is analyzed in terms of distributions of the mean streamwise velocity and the Reynolds shear stress, and profiles of the mean streamwise velocity, the streamwise velocity fluctuations, and the Reynolds shear stress. Likewise, the shock interaction case is investigated. Next, the shock interaction case is compared to the reference case before the final conclusions are drawn.

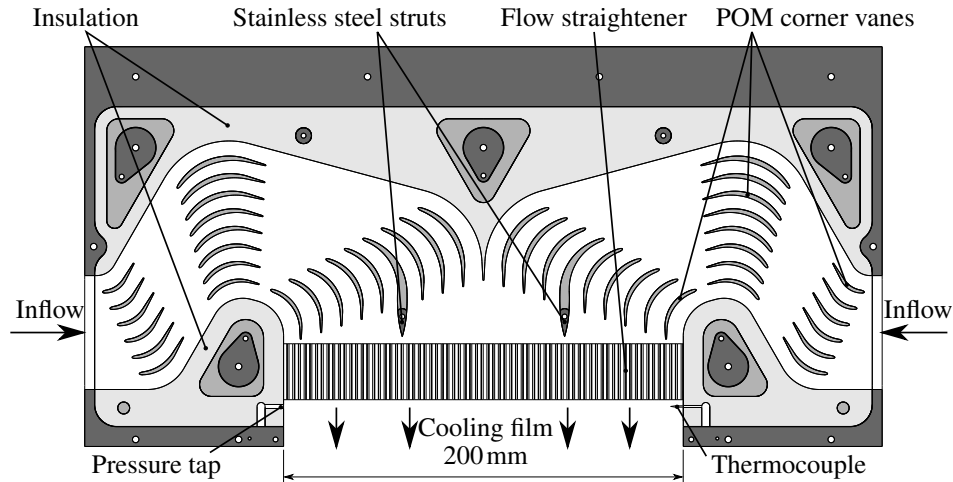


Figure 3: Spanwise cross section of the nozzle insert with plenum chamber.

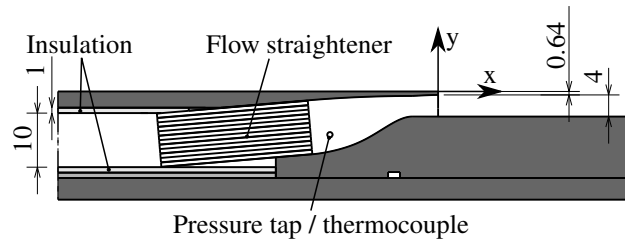


Figure 4: Cross section of the slot nozzle.

chamber are insulated with a 1 mm thick layer of rigid PVC foam. The trailing edges of two corner vanes are part of the stainless steel nozzle insert and are fixed to the bottom wall of the model. This reduces the deformation of the nozzle due to the increased pressure inside the plenum chamber. Before the flow is accelerated to the injection Mach number, it runs through a honeycomb flow straightener with a cell size of 1.6 mm and a length of 28 mm. Static pressure and temperature are monitored via a pressure tap and a thermocouple downstream of the flow straightener.

Figure 4 shows a cross section of the injection nozzle. The flow straightener is inclined by an angle of approximately 5° to reduce the amount of tracer particles impacting on the bottom part of the nozzle. The supersonic part of the Laval nozzle is realized as the upper half of a symmetric, bell-shaped nozzle. The nozzle exit height is $S = 4$ mm, and the thickness of the nozzle lip is 0.64 mm. To generate a steady cooling-film flow, the plenum chamber is fed with a constant mass flow such that the static pressure at the nozzle outlet equals the static pressure of the freestream in the wind tunnel. This constant mass flow is generated by a choked Venturi nozzle. The Venturi nozzle is fed from a bundle of twelve 200 bar helium cylinders. A pressure regulator upstream of the Venturi nozzle sets the pressure and, thus, the mass flow rate of the cooling flow. Downstream of the Venturi nozzle, the flow passes through two seeding generators with 6 Laskin nozzles each. A bypass controls the seeding density without changing the mass flow rate. The seeded cooling-film flow passes through a heat exchanger which precools the flow before it is split into two flows to enter the model symmetrically from both sides. The temperature is reduced to the final injection temperature in another pair of heat exchangers which are located close to the inlets of the nozzle insert.

The secondary sides of the heat exchangers are part of a closed-cycle cooling circuit filled with low viscosity polydimethylsiloxane (PDMS) oil. The cooling circuit is cooled by liquid nitrogen via an oil/liquid nitrogen heat exchanger. The liquid nitrogen flow rate is regulated by a closed-loop PID temperature controller to keep the temperature of the cooling circuit constant throughout the measurements. Depending on the injection Mach number and the ambient conditions, the cooling circuit is set to a temperature in the range of -55°C to -40°C .

Between two measurements, a small mass flow is fed through the helium supply to keep the plenum chamber at low temperatures, which leads to a quick transient response to a steady temperature at the begin-

ning of each measurement. With this setup, the mass flow rate and the injection temperature settle within 3 s to steady state. During the measurement time of 1.5 s, the total temperature ratio $T_{0,i}/T_{0,\infty}$ between the injection flow and the freestream flow is constant within $\pm 0.2\%$. However, variations in the temperature of the cooling circuit lead to a fluctuation of the temperature between the measurements of up to $\pm 1\%$.

2.2 Particle-image velocimetry setup and data evaluation

The particle-image velocimetry (PIV) setup consists of a Quantronix Darwin Duo 527-40-M laser and a Photron Fastcam SA5 high-speed PIV camera which are synchronized by an ILA synchronizer. The light sheet enters the test section through a window in the ceiling. It is oriented vertically and parallel to the flow on the centerline of the model (figure 2). The camera is mounted at a small angle ($\approx 2^\circ$) to the normal of the light sheet under Scheimpflug condition to reduce aero-optical aberrations. It is equipped with a 180 mm Tamron tele macro lens to realize a field of view of $30\text{ mm} \times 30\text{ mm}$ in the measurement plane. The PIV system records 1000 samples per second at a resolution of $1024 \times 1024\text{ px}^2$. The model surface is highly polished to reduce the amount of laser light scattered from the model surface into the camera. The cooling flow as well as the main flow are seeded with Di-Ethyl-Hexyl-Sebacat (DEHS). The seeding in the main flow is filtered using a cyclone particle separator that reduces the mean particle diameter. The effective particle diameter of the present setup is determined by Marquardt et al. (2019, in press). The resulting particle relaxation time of the filtered particles in the freestream is $\tau_p = 2.9\ \mu\text{s}$, and the unfiltered particles in the helium cooling film have a relaxation time of $\tau_p = 6.4\ \mu\text{s}$. This leads to a maximum relaxation length of $l_p = 1.7\text{ mm}$ in the freestream and $l_p = 5.8\text{ mm}$ in the cooling film.

Each measurement consists of 1500 snapshots recorded over a measurement time of 1.5 s. After subtraction of a background image, the particle images are preprocessed using a non-linear Gaussian blur to reduce camera noise and are dewarped using a camera calibration based on the Tsai model Tsai (1987). For the camera calibration, a CNC machined aluminum target with 0.3 mm holes filled with black paint with a spacing of 1 mm is used. Approximately 900 calibration points are used for camera calibration. To allow particle shifts larger than half the interrogation window size, the image evaluation uses a multi-grid approach with integer window shift to get an initial displacement field. The velocity field is refined using an iterative predictor-corrector scheme with subpixel accurate image deformation according to the procedure described by Astarita and Cardone (2005). The initial displacement is interpolated for each pixel of the image using a third-order B-Spline interpolation. Both images are deformed by half the displacement to get a second-order accurate estimation of the displacement field. The image interpolation uses Lanczos resampling, i.e., Lanczos windowed cardinal sine interpolation, incorporating the neighboring 8×8 pixels. An integral velocity predictor is used to ensure convergence of the iterative scheme as described by Scarano (2004). Hence, the predictor is the weighted average of the per-pixel displacement over the interrogation window. The corrector is determined by evaluating the cross-correlation function between both exposures with a 3-point Gaussian peak estimator as in Raffel et al. (2007). The initial window size for the multi-grid evaluation is $128 \times 128\text{ px}^2$ and the window size used for the iterative PIV evaluation is $32 \times 32\text{ px}^2$ with 75% overlap corresponding to a physical size of $1 \times 1\text{ mm}^2$. This leads to a final vector pitch of 0.25 mm or $0.0625S$ where S is the nozzle height. Between the iterations, outliers in the vector field are detected using a normalized median test, Westerweel and Scarano (2005), and are replaced by interpolated values. A total of three multi-grid steps and five steps of the iterative evaluation are performed, resulting in a validation rate over 90% in the final dataset. The surface reflections were masked in the recorded images, the first point used for PIV interrogation is at $\Delta y = 0.25\text{ mm}$ off the wall.

Since the field of view is approximately $30 \times 30\text{ mm}^2$ in the current setup and the cooling-film flow evolves over a considerably larger streamwise length, the results for each set of flow parameters are composed of up to nine separate overlapping measurements along the centerplane of the model. The bounds of each measurement are indicated by thin black lines in the final vector fields.

3 Results

The freestream Mach number is $Ma_\infty = 2.45$, and the freestream Reynolds number based on the nozzle height S is $Re_S = 40,500$. Cooled helium is injected beneath a turbulent boundary layer at an injection Mach number $Ma_i = 1.3$. The total temperature ratio between the freestream and the cooling-film flow is $T_{0,i}/T_{0,\infty} = 0.75$. The static pressure of the injected flow matches the freestream condition. Two cases are considered in this study. The undisturbed reference case I without shock interaction and case II with shock interaction. The shock impingement position is located at $x_{\text{imp}}/S = 52$, i.e., in the wall-jet region. The

impingement position x_{imp}/S is the intersection of the linear extrapolation of the shock and the wall. All flow parameters of this study are summarized in table 1. An estimation of the measurement uncertainties is given in Marquardt et al. (2019, in press) and the 95% confidence bounds are given as error bars in the plots.

	Ma_∞	x_{imp}	β [°]	σ [°]	p_2/p_1	Ma_i	Re_i	$M = \frac{\rho_i u_i}{\rho_\infty u_\infty}$
Case I	2.45	-	-	-	-	1.3	7,009	0.21
Case II	2.45	52	8	31	1.64	1.3	7,009	0.21

Table 1: Flow parameters.

3.1 Undisturbed flow

For undisturbed flow, i.e., no shock impinges upon the cooling film, the flow field downstream of the injection nozzle consists of the slot boundary layer on the bottom wall, the cooling film, a shear layer above the cooling film, and a mixing layer between the cooling film and the shear layer. In Figure 5 the mean streamwise velocity \bar{u}/u_∞ and the Reynolds shear stress $\overline{u'v'}/u_\infty^2$ is shown for the undisturbed reference case I. The velocity divergence is superimposed as shading to visualize the shocks and expansion waves present in the flow field. At the nozzle lip, a system of expansion waves and recompression shocks is formed when the flow is deflected around the wake downstream of the nozzle lip. Downstream of the injection nozzle, the streamwise velocity of the cooling film is considerably higher than that of the freestream. This is due to the higher speed of sound of helium compared to air which leads to a nominal injection velocity ratio of $u_i/u_\infty = 1.6$. However, the velocity of the cooling film decays downstream of the injection and approaches the value of the freestream within the field of view of the measurements. Additionally, the shear layer thickens and the velocity defect in the shear layer is decreased when the flow relaxes further downstream. The distribution of the Reynolds shear stress shows positive Reynolds shear stresses within the mixing layer between the cooling film and the shear layer. Thus, heat and momentum are transferred from the cooling film into the shear layer. Non-zero values of the Reynolds shear stress close to the bottom wall indicate the presence of a turbulent boundary which grows further downstream.

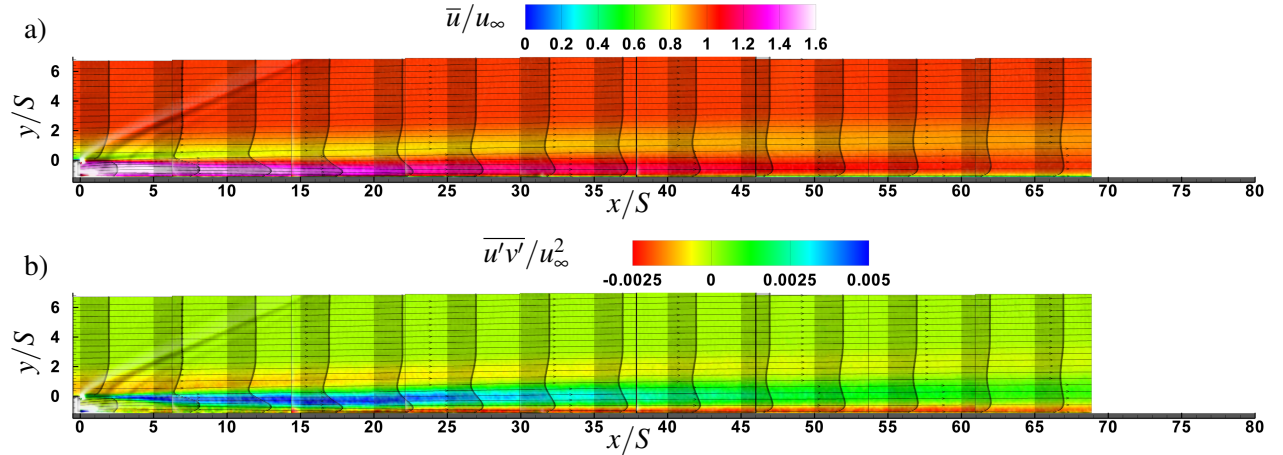


Figure 5: Mean streamwise velocity \bar{u}/u_∞ , Reynolds shear stress $\overline{u'v'}/u_\infty^2$, and profiles of the mean streamwise velocity for the undisturbed reference case I. The velocity divergence is superimposed as shading.

The development of the cooling film is shown in detail using profiles of the mean streamwise velocity \bar{u}/u_∞ , the streamwise velocity fluctuations u'_{rms}/u_∞ , and the Reynolds shear stress $\overline{u'v'}/u_\infty^2$ in figure 6. The profiles are extracted at four streamwise positions, i.e., 5, 25, 45, and 65 nozzle heights downstream of the injection position. At $x/S = 5$, the peak velocity in the cooling film equals the nominal injection velocity. The Reynolds shear stress profile does not show a region of zero Reynolds shear stress, i.e., the potential core, which indicates that the wall boundary layer and the mixing layer have already merged at this position. However, the velocity fluctuations in the center of the cooling film are as low as $u'_{\text{rms}}/u_\infty = 0.04$. The

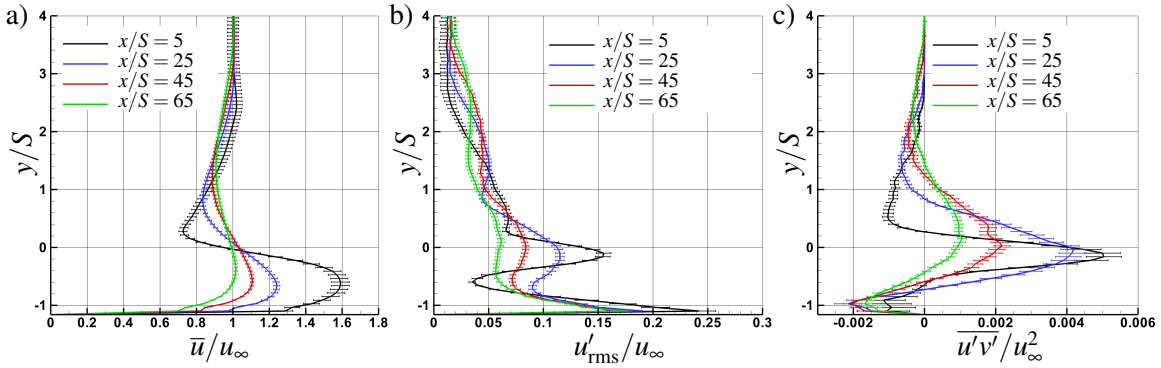


Figure 6: Profiles of the mean streamwise velocity \bar{u}/u_∞ , the streamwise velocity fluctuations u'_{rms}/u_∞ , and the Reynolds shear stress $\overline{u'v'}/u_\infty^2$ for the undisturbed reference case I at four streamwise positions.

Reynolds shear stress in the mixing layer exhibits a strong positive peak at $y/S = -0.15$ with a maximum value of $\overline{u'v'}/u_\infty^2 = 0.005$. The positive Reynolds shear stress is caused by the negative wall-normal gradient of the streamwise velocity in the mixing layer, i.e., the relatively high velocity of the cooling film compared to the freestream. As the flow develops, the peak velocity in the cooling film decreases from $\bar{u}/u_\infty = 1.6$ at $x/S = 5$ to approximately $\bar{u}/u_\infty = 1$ at $x/S = 65$. As the velocity of the cooling film decays, the positive peak of the Reynolds shear stress gradually decreases further downstream to a value of $\overline{u'v'}/u_\infty^2 = 0.001$ at $x/S = 65$. The negative peak of the Reynolds shear stress in the shear layer is reduced from $\overline{u'v'}/u_\infty^2 = -0.01$ to a value of $\overline{u'v'}/u_\infty^2 = -0.0003$ as the shear layer develops. Additionally, the peak is shifted off the wall from $y/S = 0.5$ to $y/S = 2.3$. In consequence, a large region with positive Reynolds shear stress, i.e., turbulent transport off the wall, is formed in the mixing layer which is beneficial for cooling applications.

3.2 Shock/cooling-film interaction

The distributions of the mean streamwise velocity \bar{u}/u_∞ and the Reynolds shear stress $\overline{u'v'}/u_\infty^2$ are shown in figure 7 for the shock interaction case II. The velocity divergence and mean velocity profiles are superimposed. Additionally, a solid black line indicates mean backflow and a dashed black line shows instantaneous backflow in 1% of the snapshots. The impinging shock generates a large separation bubble. The separation point is located upstream of the field of view of the measurements, i.e., at a position, where the shock generator obstructs the light sheet and no measurements could be conducted. Extrapolation of the separation bubble shape estimates the point of separation at approximately $x/S = 33 - 34$ which would result in a separation bubble length of approximately $\Delta x/S = 22 - 23$ and a thickness of $\Delta y/S = 1.5$. Unsteady separation, however, occurs in a much larger area that extends up to $\Delta y/S = 3.3$. The region above the mean separation bubble and within the unsteady separated region is characterized by high magnitudes of the Reynolds shear stress, i.e., intense turbulent mixing, that decays further downstream.

Figure 8 shows profiles of the mean streamwise velocity \bar{u}/u_∞ , the streamwise velocity fluctuations u'_{rms}/u_∞ , and the Reynolds shear stress $\overline{u'v'}/u_\infty^2$ for the undisturbed reference case I and the shock interaction case II. The profiles are extracted at $x/S = 45$ and $x/S = 65$, i.e., approximately at the position of maximum separation bubble thickness and downstream of the reattachment position. The impinging shock leads to a strong reduction of the mean velocity and a massive increase of the velocity fluctuations and the Reynolds shear stress. Compared to the undisturbed case, the velocity fluctuations in the shear layer are increased by a factor of 2 and the peak is located considerably further off the wall. The shock interaction causes negative values of the Reynolds shear stress of up to $\overline{u'v'}/u_\infty^2 = -0.06$. Thus, the Reynolds shear stress in the shear layer is increased up to a factor of 18 compared to the reference case. The mixing layer and the shear layer are deflected around the separation bubble. In the profile of the Reynolds shear stress at $x/S = 45$, the positive peak of the Reynolds shear stress in the mixing layer is apparent at $y/S = 4.2$ and the shear layer is located at approximately $y/S = 5 - 6$. When the flow reattaches, the mixing layer and the shear layer are deflected towards the wall. While the shear layer still appears at approximately $y/S = 3 - 4$ in the Reynolds shear stress profile at $x/S = 65$, the mixing layer merges with the region of strong turbulent mixing downstream of the separation bubble. Therefore, the beneficial mixing layer with turbulent transport

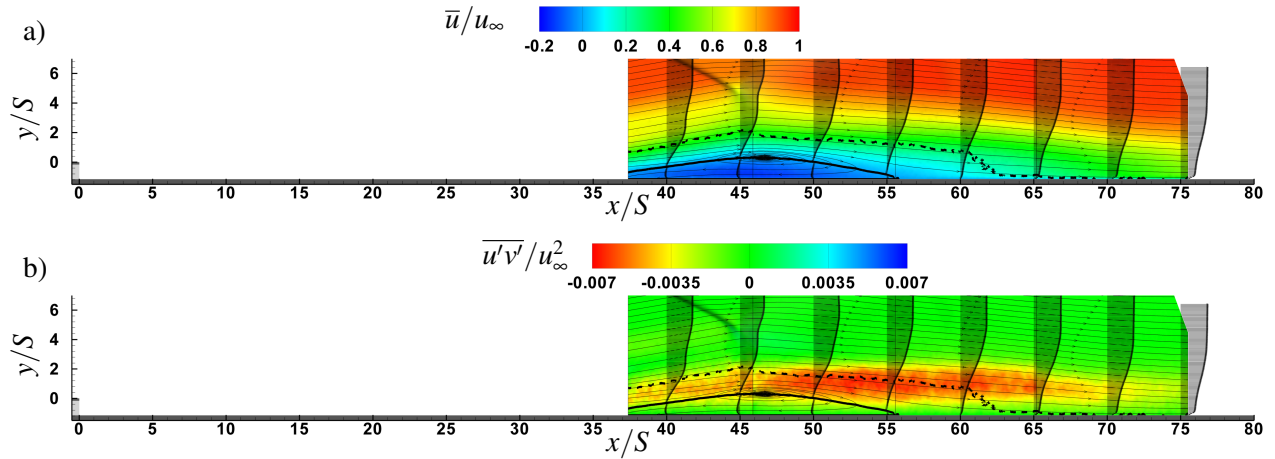


Figure 7: Mean streamwise velocity \bar{u}/u_∞ , Reynolds shear stress $\overline{u'v'}/u_\infty^2$, and profiles of the mean streamwise velocity for the shock interaction case II. The velocity divergence is superimposed as shading.

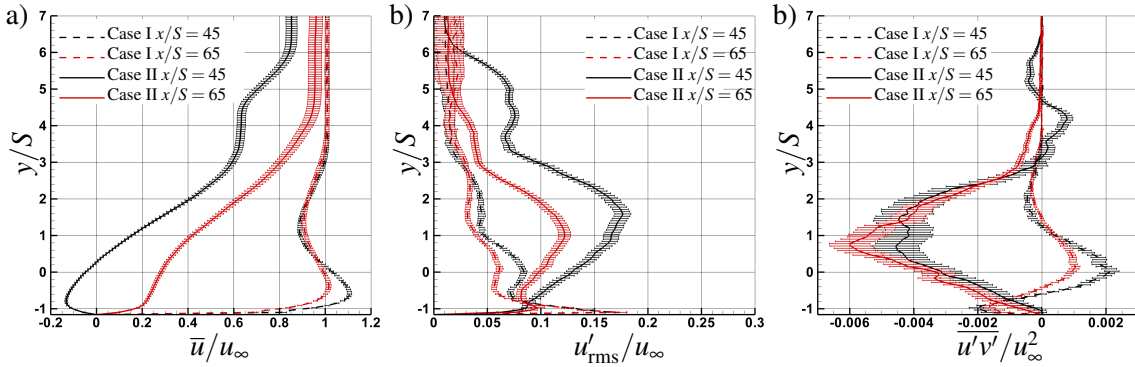


Figure 8: Profiles of the mean streamwise velocity \bar{u}/u_∞ , the streamwise velocity fluctuations u'_{rms}/u_∞ , and the Reynolds shear stress $\overline{u'v'}/u_\infty^2$ for case I and case II at two streamwise positions.

off the wall is replaced by a large region with strong turbulent transport towards the wall.

4 Conclusions

The interaction of an impinging shock and a helium cooling film was investigated by 2C high-speed PIV. The helium cooling film was tangentially injected at a Mach number $Ma_i = 1.3$ underneath a turbulent boundary layer of an air flow at a freestream Mach number of $Ma_\infty = 2.45$. The total temperature ratio between the cooling film and the freestream was $T_{0,i}/T_{0,\infty} = 0.75$. A shock was generated by a flow deflection $\beta = 8^\circ$ yielding an impingement position on the cooling film at $x_{imp}/S = 52$. In addition to the shock interaction case, a reference configuration without shock interaction was investigated.

For the no-shock problem, the high injection velocity, i.e., $\bar{u}/u_\infty = 1.6$ at the injection position, leads to a negative, wall-normal gradient of the mean streamwise velocity in the mixing layer between the cooling film and the shear layer. This causes positive values of the Reynolds shear stress. Thus, the mixing layer is characterized by turbulent transport off the wall which is beneficial for cooling purposes. The velocity of the cooling film decays further downstream and reaches values of approximately $\bar{u}/u_\infty = 1$ at $x/S = 65$ such that the intensity of the turbulent transport gradually decreases as the flow develops. The turbulent transport in the shear layer decays along the streamwise direction and the peak of the Reynolds shear stress is shifted off the wall.

With shock interaction, a large separation bubble is formed. It has a mean separation length of approx-

imately $\Delta x/S = 22 - 23$ and a mean separation height of $\Delta x/S = 1.5$. The shear layer and the mixing layer are deflected around the separation bubble. Downstream of the separation bubble, the mixing layer merges with a region of intense turbulent mixing that is formed on top of the separation bubble. Therefore, the region of turbulent transport off the wall is not present downstream of the shock induced separation bubble. Instead, the turbulent transport towards the wall is drastically increased. The peak Reynolds shear stress with shock interaction is up to 18 times higher than in the undisturbed reference case. This leads to higher thermal loads on the structures.

Acknowledgements

This research was funded by the Deutsche Forschungsgemeinschaft within the research project “Experimental Investigation of Turbulent Supersonic Film-Cooling Flows” (SCHR 309/62-1).

References

- Astarita T and Cardone G (2005) Analysis of interpolation schemes for image deformation methods in PIV. *Experiments in Fluids* 38:233–243
- Goldstein RJ (1971) Film cooling. in *Advances in Heat Transfer*. volume 7. pages 321–379
- Holden M, Nowak R, Olsen G, and Rodriguez K (1990) Experimental studies of shock wave/wall jet interaction in hypersonic flow. *AIAA Paper* 90-0607
- Juhany K and Hunt M (1994) Flowfield measurements in supersonic film cooling including the effect of shock-wave interaction. *AIAA Journal* 32:578–585
- Juhany KA (1994) *Supersonic Film Cooling Including the Effect of Shock Wave Interaction*. Ph.D. thesis. California Institute of Technology Pasadena, California
- Juhany KA, Hunt ML, and Sivo JM (1994) Influence of Injectant Mach Number and Temperature on Supersonic Film Cooling. *Journal of Thermophysics and Heat Transfer* 8:59–67
- Kamath P, Holden M, and McClinton C (1990) Experimental and computational study of the effect of shocks on film cooling effectiveness in scramjet combustors. *AIAA Paper* 90-1713
- Konopka M, Meinke M, and Schröder W (2012) Large-eddy simulation of shock-cooling-film interaction. *AIAA Journal* 50:2102–2114
- Konopka M, Meinke M, and Schröder W (2013a) Large-eddy simulation of high mach number film cooling with shock-wave interaction. *Progress in Flight Physics* 5:309–326
- Konopka M, Meinke M, and Schröder W (2013b) Large-eddy simulation of shock-cooling-film interaction at helium and hydrogen injection. *Physics of Fluids* 25:106101
- Marquardt P, Klaas M, and Schröder W (2018) PIV measurements of supersonic slot-film cooling with shock-cooling film interaction at cold injection. *19th International Symposium on the Application of Laser and Imaging Techniques to Fluid Dynamics, Lisbon, Portugal*
- Marquardt P, Klaas M, and Schröder W (2019, in press) Experimental investigation of isoenergetic film cooling flows with shock interaction. *AIAA Journal*
- Olsen GC, Nowak RJ, Holden MS, and Baker NR (1990) Experimental results for film cooling in 2-D supersonic flow including coolant delivery pressure, geometry, and incident shock effects. *AIAA Paper* 90-0605
- Raffel M, Willert CE, Wereley ST, and Kompenhans J (2007) *Particle Image Velocimetry: A Practical Guide*. Springer, Berlin Heidelberg
- Scarano F (2004) On the stability of iterative PIV image interrogation methods. *12th International Symposium on the Application of Laser and Imaging Techniques to Fluid Dynamics, Lisbon, Portugal*

Seban RA and Back LH (1962) Velocity and temperature profiles in turbulent boundary layers with tangential injection. *Journal of Heat Transfer* 84:45–54

Tsai RY (1987) A versatile camera calibration technique for high-accuracy 3d machine vision metrology using off-the-shelf tv cameras and lenses. *IEEE Journal on Robotics and Automation* 3:323–344

Westerweel J and Scarano F (2005) Universal outlier detection for PIV data. *Experiments in Fluids* 39:1096–1100